CFD SIMULATION OF THE RD-14M STEAM GENERATOR USING TWO-FLUID MODEL

Santiago F. Corzo[a]**, Dario M. Godino**[a]**, Norberto M. Nigro**[a] **and Damian E. Ramajo**[a]

[a]*CIMEC Centro de Investigación de Métodos Computacionales, UNL, CONICET, FICH, Col. Ruta 168 s/n, Predio Conicet "Dr Alberto Cassano", 3000 Santa Fe, Argentina,* `santiagofcorzo@gmail.com`*, http://www.cimec.org.ar*

Keywords: CFD, semi-scale, Seam generator, two-phase model.

Abstract. A Computational Fluid Dynamics (CFD) simulation of the secondary circuit of a steam generator test facility was carried out. The multi-phase flow was studied using the two-fluid Eulerian model. A constant boiling rate was assumed over the U-tubes walls (excepting the pre-heater) and a blending model was applied for solving the interface momentum exchange. Due to the few amount of U-tubes, geometric simplifications were avoided, thus giving a fully representation of the geometry. Steady-state conditions were simulated focusing obtain the re-circulation flow rate, the collapsed liquid level and the void distribution. Especial effort was also devoted to determinate the phase velocities, void fraction, pressure drop and the interfacial interaction inside the different parts of the steam generator. Results were in very good agreement with design nominal data.

1 INTRODUCTION

The current *NPP* typically produce thermal power larger than 2,000MWt and require 2 or 4 SGs to transfer this power to the turbine. To achieve the heat transfer each SG has between 4,000 and 10,000 U-tubes, rising heat transfer areas larger than $50,000 \ m^2$. Typical steam generators (SG) of a Pressure water Reactor (PWR) or Pressure Heavy Water Reactors (PHWR) are large vertical heat exchanger, which received heat power from the primary coolant circuit and transfer it to an isolated secondary water circuit. This kind of equipment are also found in fossil fuel thermal plants. In Nuclear Power Plants (NPP), the SGs play a significant role in many different aspects; They generate the necessary steam to impulse the turbine train but also serve as a fission product barrier to avoid the release of radionuclides and a heat sink for the primary circuit in several accidents such as Loss of Forced Convection (LFC) or Loss Of Coolant Accident (LOCA). Therefore, the study of SG both under normal operation and postulated accidents is of great importance for design enhancing as long as nuclear safety.

An sketch of a typical SG is shown in Figure 1. The primary coolant enters at high pressure and high temperature through the primary inlet, and flows along the U-tubes transferring heat to the secondary side. Finally the coolant leaves the U-tubes across the primary outlet. The secondary circuit is quite more complex; A feed water stream, generally heated outside of the SG, enters into the SG through the feed water nozzle and is heated up to saturation in the pre-heated zone. Afterwards, the saturated water is mixed in the middle of the riser with the liquid stream coming from the down-comer. The secondary circuit operates at lower pressure than the primary one to promote boiling. Near the U-tubes walls the steam bubbles nucleate, grow and finally are detached by the convective flow and local buoyancy forces. Then, bubbles rise up dragging the surrounding water and promoting agitation. Generally at the top end of the riser there is an area contraction where the steam is accelerated. Therefore, the steam drags small liquid drops towards the separation zone at the top of the SG. Separators are arrays of cyclones (primary moisture separator) in which the drops are separated from the steam by inertial forces. Subsequently, the steam crosses a dryer (secondary moisture separator), which has small orifices or parallel plates wherein the residual humidity is condensed. Finally, the steam discharged into the upper head and then it is carried to the turbine. The separated water goes down, returning to the bottom side of the riser through the down-comer, which frequently consists of an annular duct formed between the riser and the external sheet.

In SGs at less three flow patters can be identified: vapor bubbles immersed in liquid water, water droplets in vapor stream and a the transition among them. In last years, significant efforts were dedicated to study the two-phase flow model and specially to develop more realistic phenomenological models with the aim to estimate the interfacial interaction (Tomiyama et al., 2006), focusing to develop multi-scale models (Hänsch et al., 2012) (Marschall, 2011) in interpenetrating continuous models.

Even today fully geometric Computational Fluid Dynamics (*CFD*) studies for SG are still unachievable with the current computational resources. Therefore, several the authors have confronted this problem modeling the U-tubes bundle by using porous media. Stosic et. al (Stosic and Stevanovic, 2002) improved a two-fluid porous media with applications for fuel rods or shell-and-tube heat exchangers. Feng et al. (Ferng, 2007) (Ferng and Chang, 2008) studied the thermalâAŞhydraulic flow and released nuclides distribution in SGs and Rama (Rämä et al., 2010) analyzed the multiphase flow structures in horizontally disposed SGs of VVER-440 PWR-NPP. More recently, Cong et al. (Cong et al., 2013) presented a thermal-hydraulic study of the AP-1000 SG using a mixture-fluid solver with heat and mass transfer in porous media.
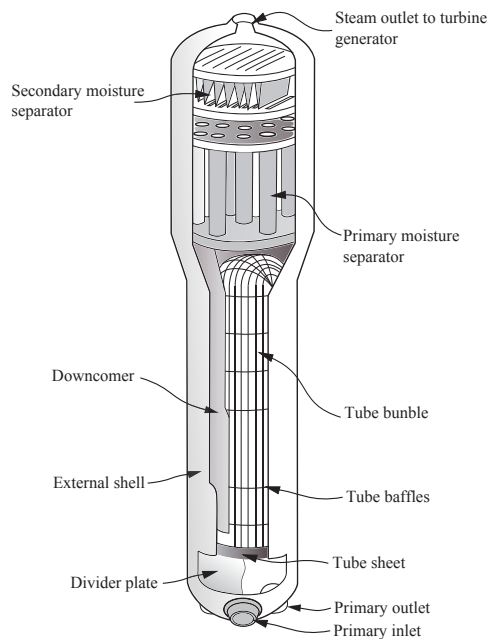
Figure 1: Steam generator components.

They also used lumped models to solve the flow in the down-comer and separators. Other contributions were performed by Li et al. (Li et al., 2013) and Zhang et al. (Zhang et al., 2014), who focused their studies in the heat transfer between the primary and secondary circuits. Li et al. carried out this using the Conjugated Heat Transfer model (*CHT*) meanwhile Zhang et al. proposed a one-dimensional (1*D*) coupled model to solve dynamic transients.

All these previous works pointed out about the variety of flow patterns, phase velocities, void distribution and pressure drops that takes place inside the SGs. However, the CFD capabilities are limited in order to simulate this complex problems; the main reasons are the amount of degree of freedom solvable by the current computational resources, the lack of understanding about the interfacial effects, the range of validity of the correlations and models and the inability of the current boiling models, among others. In this context, the CFD simulation of steam generators employing multiphase approaches, such as the two-fluid model, is a challenge.

In the current paper, the secondary side of the test facility RD14M is simulated with the two-fluid Euler-Euler model(Ishii, 1975). The geometrical characteristics of the facility allow performing a full-geometry model (FGM) in order to compare CFD results with macroscopic nominal data. For interfacial momentum exchange we proposed a blended strategy able to represent either the two extreme situations and the transition. Details of this method were given by Marschall (Marschall, 2011) and Rusche (Rusche, 2002) and briefly over-viewed in this paper.

Promoted by the saturated thermal conditions of the fluid, the problem was assumed in adiabatic conditions. The aim of this hypothesis is to avoid the issues around the mass transfer models in this kind of problems. The evaporation flow rate was assumed as a constant value distributed around the U-tubes (except in the pre-heater). The special emphasis was given to the flow interaction between the phases, the void distribution, the pressure drops and the flow structures achieved.

2   MATHEMATICAL FORMULATION

The widely known Eulerian-Eulerian two-fluid model (Ishii, 1975) (Evje and Fjelde, 2002) implemented in OpenFoam (Weller, 2002) was selected to solve the current problem. A set of equations representing the conservation of mass, momentum and energy are written for each phase and solved in order to satisfy some constraints. The interaction between phases is represented by suitable interface transfer terms that arise from constitutive relations. For a binary water-steam system the continuity equations can be written in a differential form as:

$$\frac{\partial(\alpha_1\rho_1)}{\partial t} + \nabla \cdot (\alpha_1\rho_1\mathbf{U_1}) = \Gamma_1 \tag{1}$$

$$\frac{\partial(\alpha_2\rho_2)}{\partial t} + \nabla \cdot (\alpha_2\rho_2\mathbf{U_2}) = \Gamma_2 \tag{2}$$

where the sub-indexes 1 and 2 indicate water and steam phases respectively, α denotes the volume fraction, ρ the density and $\mathbf{U}$ the velocity. The terms Γ_1 and Γ_2 in the right hand side are the net mass transfer accounting for evaporation and condensation. By adding both mass equations the total mass conservation is obtained. This global balance equation becomes a restriction to be satisfied for the pressure-velocity coupling (Weller, 2002). The difference between the evaporation and condensation rates is the net mass transfer of each phase. That is: $\Gamma_1 = \Gamma_{1,2} - \Gamma_{2,1}$ and $\Gamma_2 = \Gamma_{2,1} - \Gamma_{1,2}$. Despite of $\Gamma_1 = -\Gamma_2$, the net interfacial mass transfer must be zero. Finally, the total mass conservation equation is:

$$\frac{\partial(\alpha_1\rho_1)}{\partial t} + \frac{\partial(\alpha_2\rho_2)}{\partial t} + \nabla \cdot (\alpha_1\rho_1\mathbf{U_1} + \alpha_2\rho_2\mathbf{U_2}) = 0 \tag{3}$$

The conservation of momentum is accomplished by one momentum equation for every phase. However, all of them are coupled through the interfacial force terms. Using the Reynolds time-average (Reynolds, 1895), the two conservation momentum equations are written as:

$$\frac{\partial(\alpha_1\rho_1\mathbf{U_1})}{\partial t} + \nabla \cdot (\alpha_1\rho_1\mathbf{U_1}\mathbf{U_1}) =$$

$$-\nabla \cdot (\alpha_1(\tau_1 + R_1)) - \alpha_1\nabla p + \alpha_1\rho_1\mathbf{g} + \mathbf{M_1} + (\Gamma_{2,1}\mathbf{U_2} - \Gamma_{1,2}\mathbf{U_1}) \tag{4}$$

$$\frac{\partial(\alpha_2\rho_2\mathbf{U_2})}{\partial t} + \nabla \cdot (\alpha_2\rho_2\mathbf{U_2}\mathbf{U_2}) =$$

$$-\nabla \cdot (\alpha_2(\tau_2 + R_2)) - \alpha_2\nabla p + \alpha_2\rho_2\mathbf{g} + \mathbf{M_2} + (\Gamma_{1,2}\mathbf{U_1} - \Gamma_{2,1}\mathbf{U_2}) \tag{5}$$

here τ is the laminar stress tensor and R is the Reynolds stress tensor. p is the pressure and M_1 and M_2 are the interfacial forces per unit volume. As noted, in this formulation the same pressure is shared by both phases. Based on the assumption that there exists analogy between laminar viscous stresses and Reynolds stresses, the Reynolds tensor becomes proportional to the laminar stress tensor, which is defined for each phase γ ($\gamma = 1$ for water and $\gamma = 2$ for steam) as:

$$\tau_\gamma = -\rho_\gamma\nu_\gamma[\nabla\mathbf{U}_\gamma + \nabla^T\mathbf{U}_\gamma] + \frac{2}{3}\rho_\gamma\nu_\gamma(\nabla \cdot \mathbf{U}_\gamma)I \tag{6}$$

where ν_γ is the molecular kinematic viscosity and I is the identity matrix. Finally, R_γ is given by the following expression:

$$R_\gamma = -\rho_\gamma \nu_{\gamma,t}[\nabla \mathbf{U}_\gamma + \nabla^T \mathbf{U}_\gamma] + \frac{2}{3}\rho_\gamma \nu_{\gamma,t}(\nabla \cdot \mathbf{U}_\gamma)I + \frac{2}{3}\rho_\gamma \kappa_{\gamma,t}I \tag{7}$$

where $\kappa_{\gamma,t}$ is the turbulent kinetic energy, and $\nu_{\gamma,t}$ is the turbulent kinematic viscosity.

To obtain the phase fractions α_1 and α_2 it is enough to solve either equation 1 or 2. Generally, the continuity equation for the dispersed phase is solved and the other phase is obtained by the restriction $\alpha_1 + \alpha_2 = 1$. Following the method proposed by Weller et al. (Weller, 2002), the continuity equation 1 is rewritten to avoid boundlessness problems. Thus, rewriting the phase velocity in terms of the mean and relative velocities $\mathbf{U}$ and $\mathbf{U_r}$:

$$\mathbf{U} = \alpha_1 \mathbf{U_1} + \alpha_2 \mathbf{U_2} \tag{8}$$

$$\mathbf{U_r} = \mathbf{U_1} - \mathbf{U_2} \tag{9}$$

Let us:

$$\mathbf{U_1} = \mathbf{U} + \alpha_2 \mathbf{U_r} \tag{10}$$

Substituting Eq. 10 into the phase continuity equation 1 leads to:

$$\frac{\partial(\alpha_1 \rho_1)}{\partial t} + \nabla \cdot (\alpha_1 \rho_1 \mathbf{U}) + \nabla \cdot (\alpha_1 \alpha_2 \rho_1 \mathbf{U_r}) = \Gamma_{1,2} - \Gamma_{2,1} \tag{11}$$

A two-equation model is used to evaluate the Reynolds stress tensor (R) in equation 7. In multi-phase problems the turbulence calculation with the $k - \varepsilon$ model is commonly carried out only for the continuous phase and then inferred for the dispersed phase throw response coefficients. However, this methodology presents several limitations in practice. In recent years, Behzadi (Behzadi et al., 2004) proposed a mixture $k - \varepsilon$ formulation to solvable the mentioned issue:

$$\frac{\partial}{\partial t}(\rho_m k_m) + \nabla \cdot (\rho_m \mathbf{U_m} k_m)$$

$$= \nabla \cdot \left(\frac{\mu_{m,t}}{\sigma_{k,m}}\nabla k_m\right) + P_k{}^m - \rho_m \varepsilon_m + S_k{}^m \tag{12}$$

$$\frac{\partial}{\partial t}(\rho_m \varepsilon_m) + \nabla \cdot (\rho_m \mathbf{U_m} \varepsilon_m) = \nabla \cdot \left(\frac{\mu_{m,t}}{\sigma_{\varepsilon,m}}\nabla \varepsilon_m\right)$$

$$+ \frac{\varepsilon_m}{k_m}(C_{\varepsilon 1}P_k{}^m - C_{\varepsilon_m 2}\rho_m \varepsilon_m + C_{\varepsilon_m 3}S_\varepsilon{}^m) \tag{13}$$

where k and ε are the turbulent kinetic energy and turbulent dissipation rate and the sub-index m refers to the mixture. Standard values are assumed for the turbulent parameters ($C_\mu = 0.09$, $C_{\varepsilon 1} = 1.44$, $C_{\varepsilon 2} = 1.92$, $C_{\varepsilon 3} = 1.92$, $\sigma_{k,m} = 1.0$ and $\sigma_{\varepsilon,m} = 1.3$). The source terms in Eq. 12 and 13 are computed such as was proposed by Lahey (Lahey, 2005).

The mixture properties are related to the phase properties by mean of a response coefficient C_t ($C_t{}^2 = k_d/k_c = \varepsilon_d/\varepsilon_c$). This coefficient stands for the ratio between the dispersed phase velocity fluctuations and the continuous one. Based on experimental results Behzadi(Behzadi

et al., 2004) suggested that the turbulence response coefficient is strongly influenced by the phase fraction α_d and he proposed the following relationship:

$$C_t^2 = 1 + (C_{t0} - 1)e^{-f(\alpha_d)} \tag{14}$$

where

$$f(\alpha_d) = 180\alpha_d - 4.71 \times 10^3 \alpha_d^2 + 4.26 \times 10^4 \alpha_d^3 \tag{15}$$

Hill(Hill, 1998) defined the coefficient (C_{t0} as function of the local flow and the turbulence fields:

$$C_{t0} = \frac{3 + \beta}{(1 + \beta + 2\rho_d/\rho_c)} \tag{16}$$

$$\beta = \frac{6C_\mu}{(4*(3/2)^{1/2}} \frac{C_{D,d}}{\rho_c} \frac{k_c}{\varepsilon_c} \tag{17}$$

where the sub-indexes d and c refer to discrete and continuous phases. $C_{D,d}$ is the drag coefficient.

The mixture fields k_m, ε_m, $\mathbf{U_m}$, $\mu_{m,t}$ are computed with "pseudo-mass-weighted" average between both continuous and dispersed phases.

Finally, the turbulent kinetic energy κ_γ and turbulent dissipation rate ε_γ for each phase are recovered from the C_t and the turbulent viscosity $\mu_{t,\gamma}$ is obtained from the widely known relationship:

$$\mu_t = C_\mu \frac{k_\gamma}{\varepsilon_\gamma} \tag{18}$$

Interfacial Momentum exchange

Different mechanisms of interfacial momentum transfer have been discussed in the past, frequently by studying the dimensionless equations of motion and making comparisons with experimental data (Enwald et al., 1996). From these precursor studies, it was concluded that the net interfacial force can be divided on several independent physical effects:

$$M_{1,2} = -M_{2,1} = M^D + M^{SL} + M^{WL} + M^{VM} + M^{TD} \tag{19}$$

In Eq. 19 the term M^D represents the drag force, M^{SL} is the lift force, M^{WL} is the wall-lubrication force, M^{VM} is the virtual mass force and M^{TD} is the turbulence dispersion (Pellacani et al., 2010).

All these terms play a crucial role in the SG flow. Therefore, especial attention should be taken to define the proper models. In addition, different flow regimes can be identified along the SG (see Figure 2):

a) *Liquid with small bubbles nucleated at the U-tubes walls.* The **bubbly** regime occurs at the bottom of the riser with very small void fractions. The flow is characterized by small spherical bubbles moving in liquid continuous flow. Bubbles move very slowly with little interaction among them (Mostafa, 2008).

b) *Liquid with bubbles nucleating, growing and detaching from the U-tube walls.* The void fraction increases and bubbles begin to coalesce giving less but larger bubbles (**slug** regime). The interaction among phases gets significant.

c) *Steam with drops.* Due to the density ratio among phases, high steam velocity occurs in the top of the riser. The steam leaving the riser drags drops with different sizes. The motion is governed by drag and gravity forces.

d) *Steam with fine droplets.* Because of the high efforts, the largest drops break up into small droplets before to enter the separators.

e) *Separated flow.* Inside the separator the drops are forced to hit the walls induced by centrifugal effects. Due to the impacts and frictions the drops lose part of the kinetic energy and form slugs, which fall down by gravity.

Summarizing, the two-phase flow inside the SG pass through different regimes along the secondary circuit. In the bottom of the riser (*a*), the liquid is the continuous phase and the steam appears as small bubbles. Meanwhile, in the upper zone (*c*) the steam is the continuous phase and the liquid is found as drops or slugs. For this reason, consider that one phase is continuous everywhere seems to be a mistake.

The non-drag forces play a significant role in this kind of problems. e.g., the shear-induced and wall-Induced lift force promotes the agitation of the fluid close to the U-tubes and the Wall-Induced lift force detaches the vapor from the walls and increases the bubbly nucleation.
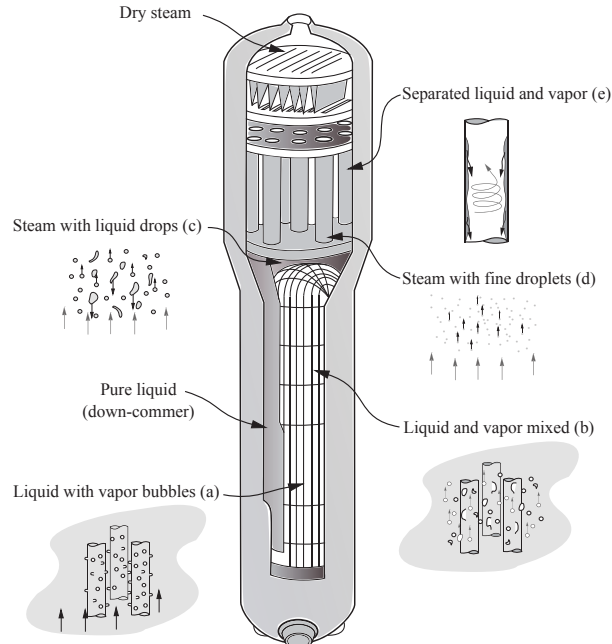

Figure 2: Computational domain.

2.1 Blending model for phase coupling

As mentioned, the liquid and steam phases take the continuous and dispersed roles depending on the place where they are. Therefore, it is necessary to have suitable models for bubbles

moving in water and for drops moving in steam. For achieving that a blending strategy with linear transition between both models was adopted. This allows affecting all the interfacial forces (Eq. 19) by three functions; f_1 : corresponding to bubbles fully dispersed in water. f_2 : corresponding to drops fully dispersed in steam and f_{tran} accounting for the transition. The three functions are defined as:

$$\alpha_1 \le \alpha_{fd} \begin{cases} f_1 = 1.0 \\ f_2 = 0.0 \end{cases} \tag{20}$$

$$Transition \begin{cases} f_1 = \frac{\alpha_1 - \alpha_{fd}}{\alpha_{pd} - \alpha_{fd}} \\ f_2 = \frac{\alpha_{fd} - \alpha_2}{\alpha_{pd} - \alpha_{fd}} \end{cases} \tag{21}$$

$$\alpha_2 \ge \alpha_{pd} \begin{cases} f_1 = 0.0 \\ f_2 = 1.0 \end{cases} \tag{22}$$

where α_{fd} and α_{pd} refers to the fully-dispersed and partially-dispersed limits for which the transition starts and finishes. The model limits were set by default as $\alpha_{fd} = 0.3$ and $\alpha_{pd} = 0.5$ Finally, each one of the interfacial force terms in Eq. 19 will be affected by an effective coefficient K^i_{eff} which is calculated by:

$$K^i_{eff} = K^i_{1,2}(f_1 - f_2) + K^i_{1d}(1 - f_1) + K^i_{2d}f_2 \tag{23}$$

where $K^i_{1,2}$ corresponds to the coefficient for mixed flow, and K^i_{1d} and K^i_{2d} are the coefficients for fully-segregated flow. The supra-index i refers to D, SL, WL, VM or TD. That is, there is a set of coefficients for each kind of interfacial force term. These three coefficients are defined in follows sections for the different interfacial forces.

2.2 Drag force

This force represents the resistance opposed to the motion of bubbles, drops and particles in the continuous fluid. The drag force typically has a quadratic dependency with the relative velocity among phases, tending to equalize their velocities. Moreover, for dispersed-continuous systems, it is strongly dependent upon the shape and size of the disperse phase as long as the flow regime. In the past, detailed studies were conducted by Clift (Clift et al., 1978) and Ishii(Ishii and Zuber, 1979) finding that the main parameters characterizing the flow regime are the Eotvos number ($E_o = \frac{d_d^2 g \Delta \rho}{\sigma_c}$), the Morton number ($M_o = \frac{\mu_c^4 g \Delta \rho}{\rho_c^2 \sigma_c^3}$) and the bubble Reynolds number ($Re_d = \frac{\rho_c d_d U_r}{\mu_c}$). Figure 3 shows the different regimes for bubbles rising in continuous media(Clift et al., 1978). The terminal velocity (or the relative velocity U_r) can be estimated directly from the Re_d by knowing the E_o and M_o ($Re_d^2 = \frac{4}{3C_D}\sqrt{\frac{E_o^3}{M_o}}$) ((Tomiyama et al., 1998)). Similarly, the drop shape regime can be defined by knowing two of the three dimensionless numbers. Figure 3 was built from experimental test data for bubbles rising freely in a continuous stagnant fluid. Furthermore, the majority of the drag models have been derived from these experimental data. However, in general the engineering applications are farther than these ideal situations and the interaction among particles play a crucial role.

Returning to Eq. 19 the drag effort M^D is modeled as:

$$M^D = \frac{3}{4}\alpha_d \frac{\rho_c \nu_c}{d_d} C_D Re_d(\mathbf{U_c} - \mathbf{U_d}) \tag{24}$$

Figure 3: Different regimes for bubbles rising in stagnant fluid pool.

where C_D is the drag coefficient, which for rigid particles is generally computed only as a function of Re_d. Perhaps the more widely employed for spherical particles is the Schiller and Naumman (Schiller and Naumann, 1933) model, which also considers that no any particle-particle interaction takes place. On the other hand, many empirical and semi-empirical equations have been proposed to calculate the C_D for non-rigid bubbles or drops moving in continuous media (Clift et al., 1978). Referenced models are by Wen Yu(Gidaspow, 1994), Ishii-Zuber(Ishii and Zuber, 1979) and Tomiyama. They have some corrections to account for particle deformation and interaction among particles. In this work, the Tomiyama model was selected for describing both bubbles moving in water and drops moving in steam. This model considers bubble or drop distortion but additionally contains a parameter accounting for the contamination of the continuous media.

Tomiyama model

Tomiyama et al. ((Tomiyama et al., 1998)) quantified the drag effect for several regimes (spherical and non-spherical shape) in pure (double distillate water), slightly contaminated (single distillate water) and contaminated (no distillate water) systems. They concluded that for fine spherical bubbles the governing effect is the viscosity and drag is dominated by the Reynolds of the bubble (Re_b). On the other hand, for non-spherical shape bubbles the surface tension and the gravity became dominant. Thus, the drag dependents on E_o. The Eq. 25 accounts for the both cases:

$$C_D = \max \left(A.\min \left(1 + 0.15 Re_d^{0.687}, 3 \right), 8 R_d \frac{E_o}{3 E_o + 12} \right) \quad (25)$$

where A is a parameter which changes from 16 for pure water to 24 for slightly contaminated water. Despite of Tomiyama model is suitable both for drops and bubbles, it was chose to estimate the drag coefficients in all situations. That is, bubbles in water (K_{1d}^D), drops in steam (K_{2d}^D) and the transition ($K_{1,2}^D$) in Eq. 23. Despite of the same drag model was used for all situations, the advantage of the blending model was to differentiate the flow properties, specially in the estimation of the Bubble/Droplet Reynolds (Re_b). This concept is explained below. Other

capability of the blending is the introduction of different sizes for drops and bubbles.

In order to improve the study, the drag effect was analyzed macroscopically in a simple test. Like mentioned above, this problem present two main flow structures. In the SG raiser the vapor behaves as a dispersed phase. In the other hand, in the separator, the vapor represent the continuous phase. The assumption of an specific continuous phase induce to a mistake. The main error occur in the bubbly/droplet Reynolds estimation. To understand this problem, the picture in figure 4 sketches the domain test. This correspond to a little portion of the second stage of the SG separator (Its description will give below). Basically, there are 4 mouthpieces that inject the steam stream with the dragged water droplets. The water impact in the external shell and drop down. For this problem we assume the 2 Kg/s vapor mass flow rate with an extreme quantities of water (1 Kg/s). This mass flow rates was affected by the adopted mouthpieces ratio (4/96). A steam must leave the domain throw the upper patch, meanwhile the liquid is leaved by an orifice in the lower patch. The water level avoid the steam discharge throw the lower orifice. The same RD-14 mesh features was assumed for this domain. Two appropriated drag models was adopted to the analysis: the Tomiyama and Schiller-Naumann models. Both models was assessed assuming the vapor as the continuous phase and dispersed phase.

Figure 4 shows the liquid mass flow rate throw the upper patch. The expected value must be very close to 0. The cases where the vapor is assumed as continuous phase (VC) present good efficiency with low liquid drag to the upper outlet. The behavior is similar to the expected. The liquid is accumulated in the wall and fall down by the gravitation effect. Regards the other case where the liquid is assumed as continuous phase (LC) the separation effect is not achieved. The drag phenomena dominates the problem and the liquid is dragged even in the wall. In this sense, the 80% of the mass water leave the domain dragged by the vapor stream. The large drag induce a fully mixing in the domain and both phases can not be identified. The main difference between both liquid-vapor configurations lies in the bubble/droplet Reynolds ($Re_d = \frac{\rho_c d_d U_r}{\mu_c}$). The fluid properties plays the main role. When the liquid is assumed as continuous phase, the large Re_b induces highs drag forces (Despite of the lower drag coefficient) and dominates over the wall-induced drag. To conclude, both assessed drag coefficient models do not show significant differences.
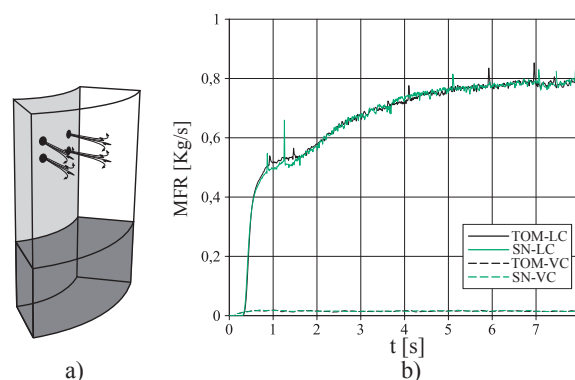

Figure 4: Drag test facility: a. Domain features, b. Liquid mass flow rate trow the steam outlet.

To complete the drag study, several liquid droplets diameters was assessed in the above presented test. The same flow ratio was assumed (2Kg/s of vapor with 1Kg/s of liquid). The vapor was assumed as continuous phase. Table 1 summarizes the separation efficiency. It must be noted that the efficiency is good for all cases and the droplet diameter has not significant

effect under this conditions. For the lowest diameters the efficiency decreases. It is expected because the finer drops are dragged by the vapor stream.

	Tomiyama	Schiller-Naumann
d_l [mm]	ε [%]	ε [%]
0.2	99.08	93.29
1	99.02	99.42
5	99.36	99.86

Table 1: Dryer efficiency for both Tomiyama and Schiller-Naumann drag model and different water droplets diameters

Based on the presented results, the blending strategy is of fundamental importance for the problem. A water droplet diameter of 1mm was adopted. Regards the vapor bubble diameter, the literature (Tolubinsky and Kostanchuk, 1970) (Unal, 1976) give values of bubble lower than 1mm. This correlations studied the bubble generation in the heated wall and the maximum diameter reached in the detachment. The flow behavior in the SG is quite different and the expected diameters are larger than these values. The fully evaporation induce the coalescence of higher bubble. For this reason, in the present work 2mm was assumed for the vapor bubble diameter.

2.3 Virtual mass Force

Virtual or added mass force (M^{VM}) is an extra resistance force due to the relative acceleration of one phase with respect to the other. This force tends to equalize the acceleration of both phases. This force is neglected when the dispersed phase has a larger density than the continuous one (eg. drops in air), but takes relevance on the contrary situation. M^{VM} is calculated by the widely used correlation (Drew and Passman, 1999):

$$M^{VM} = \alpha_1 \alpha_2 C_{VM} \rho_c \left(\frac{DU_d}{dt} - \frac{DU_c}{dt} \right) \tag{26}$$

where C_{VM} is the virtual mass coefficient, ρ_c is the density of the continuous phase and $\frac{DU_d}{dt}$ and $\frac{DU_c}{dt}$ are the velocity material derivatives for the discrete and continuous phases. C_{VM} is commonly defined with a constant value of 0.5(Sar et al., 2009) independently of the flow regime. The same value was assumed for all the blending model coefficients ($K_{1d}^{VM} = K_{2d}^{VM} = K_{1,2}^{VM}$).

2.4 Shear-Induced lift force

The lift force (or shear-induced lift force) appears when a particle moves in a continuous fluid which has shear stress, specially entailed by the walls. This force acts in orthogonal direction with respect to the particle motion. Therefore, it plays an important role on the radial distribution for low density particles moving in high density fluids (eg. bubbles in water flowing in a vertical duct). This force impulse the particles toward or far to the walls. The lift force is calculated from potential flow theory as (Drew and Lahey Jr, 1987):

$$M^{SL} = \alpha_1 \rho_2 C_L U_r \times (\nabla \times U) \tag{27}$$

where C_L is the dimensionless lift coefficient. Several empirical correlations was proposed in the past(Tomiyama, 2004)(Frank et al., 2008). This coefficient can take values between 0.01 to 0.5(Wang et al., 1987). Based on Antal et al. results (Antal et al., 1991), we assumed $C_L = 0.1$. The same value was defined for the three blending coefficients.

2.5 Wall-Induced lift force

This force, also named wall-Lubrication force, acts normally to the particle trajectory and becomes significant near the walls, pushing the particles outwards the wall. The effect of the wall induced lift force is significant for bubbles moving in liquid media but it becomes negligible for drops in gas media. In this work, the model proposed by Antal et al. (Antal et al., 1991) was implemented in OpenFoam:

$$M^{WL} = \alpha_1 \rho_2 C_{WL} \mid \mathbf{U} \mid^2 \mathbf{n_w} \tag{28}$$

where $\mathbf{n_w}$ is the unit normal vector and C_{WL} is the wall lubrication coefficient, which is computed as:

$$C_{WL} = \frac{Cw_1}{d_1} + \frac{Cw_2}{y_w} \tag{29}$$

In Eq. 29 y_w is the bubble to wall distance. $Cw_1 = -0.104 - 0.06 \mid \mathbf{U_r} \mid$ and $Cw_2 = 0.147$.
M^{WL} is significant only within a thinner region near the wall ($y_w \leq -(Cw_2 d_1/Cw_1)$). This model was originally based on experimental data for adiabatic conditions (without bubble nucleation on the walls). However, Konkar et al. (Koncar and Mavko, 2004) and Krepper et al. (Krepper et al., 2007) reported that the model is also suitable for subcooled boiling systems by taking model constants $Cw_1 = -0.025$ and $Cw_2 = -0.075$.

3 COMPUTATIONAL MODELS

The RD-14M is a test facility, which has similarity from the point of view of thermo-hydraulics parameters. It contains only two of the four coolant loops of the real CANDU reactors. Each loop has a SG and a centrifugal pump. The reactor core consists of ten channels, which are electrical heated delivering a total thermal power of 11 MW. This facility was designed to operate with the same pressure and temperature ranges, mass flux and enthalpy distribution than real CANDU units. This allows studying the response of the unity under fast transient and postulated accidents. The table 2 compares the main flow conditions and constructive characteristics of the RD-14M and the CANDU 6 reactors.

Each SG houses a vertical U-tube bundle with 44 tubes with an average height of 9.4m (Incoloy-800). Tubes have an external diameter of 15.88mm and thickness of 1.13mm. The SG has only one cyclone separator, housed in the top-head and covered by a thin shell perforated dryer for the secondary moisture separation. The maximum thermal power is 5.5 MW per SG. The coolant inlet temperature is 295°C and the expected outlet temperature is 264°C. At nominal conditions the recirculating ratio is 5 : 1, which is a bit lower than for CANDU units. Figure 5 shows the SG geometry. A view of the counter-flow pre-heater is shown at the bottom left side. At the middle, one of the 13 support sheets is featured. These sheets obstruct the central flow, forcing the stream to pass throw the peripheral side of the U-tube bundle. In the figure the central vertical bane is also shown. This component divides the riser in two zones: one for the feed water stream and other for the re-circulation flow. However, there are 5 by-pass in the bane for pressure equalization with also allow flow mixing between both sides. Finally,

Characteristic	CANDU-6	RD-14M
Amount of loops	4	2
Amount of SGs/Pumps	4	2
Amount of Channels	380	10
Thermal power (*MW*)	2109	11
Electric power (*MW*)	648	-
Coolant mass flow per loop (*kg/s*)	1900	24
Secondary mass flow per SG (*kg/s*)	235	2
Amount of U-tubes	3540	44
Outside diameter of the U-tubes (*mm*)	15.9	15.9
Tube Wall Thickness (*mm*)	1.13	1.13
Average tube Bundle Height (*m*)	9.42	9.4
Overall Height SG (*m*) SG	18.7	12
Recirculation Ratio (full power)	5.7:1	5:1
Coolant Pressure (*MPa*)	10	10
Coolant Temperature (°*C*)	310	310
Secondary Pressure (*MPa*)	4.5	4.5
Feedwater Temperature Secondary (°*C*)	187	187

Table 2: Comparison between CANDU-6 and RD-14M.

a view of the separation zone is shown at the upper-left-side picture. Meaningful effort was done to represent the real geometry, including all the U-tubes, baffles and support sheets. The cyclone separator and the perforated cup drilling dryer were also included.

The domain was meshed using a dedicated hybrid combination between structured and unstructured grids. The overall mesh demanded $10,219,505$ cells ($4,616,953$ tetrahedra, $5,468,202$ pentahedra, $10,800$ hexahedra and $123,550$ pyramids). Figure 6 shows mesh details around the separator zone. The whole riser and the dryer outside were meshed with structured grids whereas the U-tubes bend, the cyclone and the upper side of the top-head were meshed using unstructured grids. To avoid difficulties, the five cylindrical holes in the central vane were represented by square holes of the same cross section area. It allows structured meshing.

The two-fluid solver uses the Multidimensional Universal Limiter with Explicit Solution (MULES) (Zalesak, 1979) (Márquez Damián, 2013) to solve the continuity equation. Linear algorithms was used for the momentum and pressure equations. Regarding the steam generation, the solver was modified to include the mass evaporation rate $\Gamma_{1,2}$. $\Gamma_{1,2}$ was imposed at the U-tube walls with the exception of the pre-heater zone, in which evaporation was dismissed. To accomplish that, the nearest cells close to the U-tubes walls where identified and a constant value (per volume) for Γ, which ensure the overall evaporation rate, was imposed. An ad-hoc restriction had to be included to guaranty mass conservation in those cells for with the void fraction exceed unity. On the other hand, the condensation mass transfer ($\Gamma_{2,1}$) was neglected. A first order scheme was used to discretize the divergence terms. As above mentioned, the primary to secondary heat transfer and the heat exchange amount phases were not solved in the
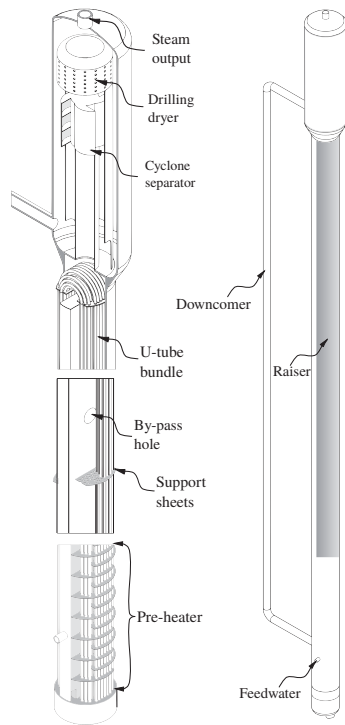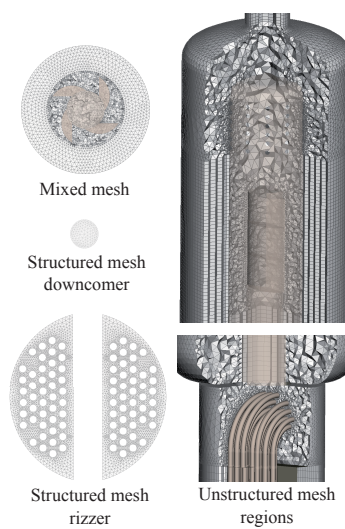
Figure 5: RD14 steam generator details.

Figure 6: Mesh details.

present model.

The initial conditions, specially for the phase distributions, were carefully defined to reach more quickly the steady-state conditions. The run was performed in parallel distributed computing using 64 cores (E5-1660-v3, 26GB-RAM DDR3, 160GBHD, Infiniband QDR4 Gbps). Despite of that, around 70 days of simulation were required to get only 16 sec of real time. However, this short time was enough to reach steady solutions for the liquid level and the outlet steam mass flow.

4 RESULTS AND DISCUSSION

In this section the results for steady-state operation are presented. An exhaustive description of the void distribution, phase velocities and pressure drops is done in order to display those flow characteristics, which are unable from system code models or experimental observation.

4.1 Macroscopic results

One of the more relevant parameters that characterize SGs is the re-circulation rate (m_{re}= $\frac{m_w}{m_s} = 5$). In single phase systems, re-circulation is due to density changes promoted by local heat transfer. On the contrary, in SGs the driven force is mainly due to the mixture in the riser has a lower weight than the liquid in the downcomer. In this SG the steam flows ($m_s = 2Kg/s$) dragging ups liquid ($m_w = 10Kg/s$) towards the separator cyclone. m_{re} is directly affected by the pressure drop along the secondary side and the steam velocity because on the interfacial forces. Figure 7-a shows the evolution of the re-circulation flow during the beginning of run. As noted, after 11 sec the m_{re} reaches the expected value. Figure 7-b shows the mass flow rate of steam (red line) and water (blue line) leaving the riser. The left scale corresponds to water and the right scale is for steam. Both of them display significant fluctuations around the nominal values, although the steam mass flow seems to be a bit higher than the expected.

It must be highlighted the good accordance between CFD results and the nominal data. As noted from Figure 7, the steady state solution is reached after a transient, which seems to be short in terms of real time but is very long in terms of computational time. It should be mentioned, that the initialization of the current model plays a crucial role. For example, if the total evaporation rate is imposed since the beginning of run with the riser fully filled with liquid, the "swelling" effect is observed. That is, the steam blow ups the riser and quickly push ups the liquid causing significant over pressure at the cyclone entrance. This high pressure at the top of the riser induces liquid counter flow through the downcomer. To mitigate this phenomenon, suitable initial conditions for the steam fraction as long as an slow evaporation rate slope are needed.

4.2 Flow elds

Figure 8 shows the main variable fields over a mid-plane cutting the riser. For clarity the real aspect ratio of the riser was modified. The first picture (figure 8) shows the void fraction; note that in the bottom side of the right leg (which houses the pre-heater) there is not steam. On the contrary, for the left zone the evaporation takes place from the bottom. The saturated liquid stream coming from the down-comer is quickly mixed with the steam in the early stages of the riser.

Despite the steam migration from the left leg to the right leg through the five connection holes, the top side of the left leg contains more steam than the other. The baffles promotes the accumulation of steam below them, whereas the liquid accumulates over the baffles.
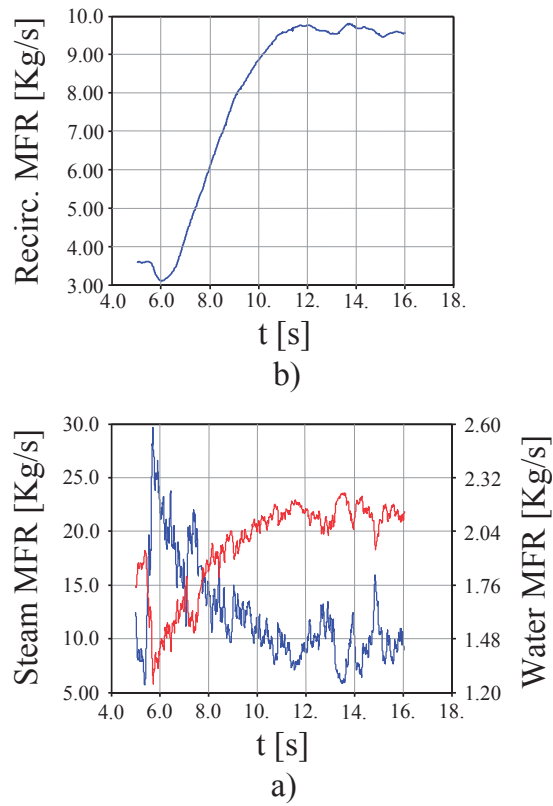
Figure 7: a) Mass flow rates of water and steam leaving the riser, b) Re-circulation mass flow rate.
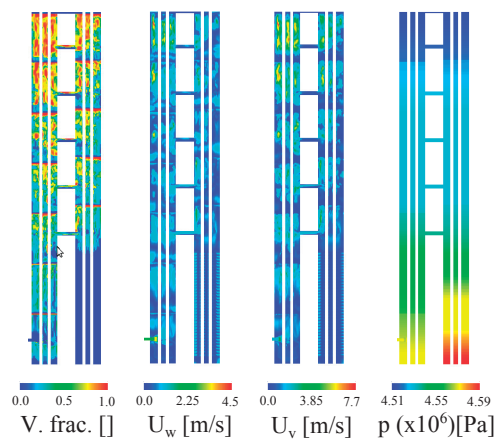

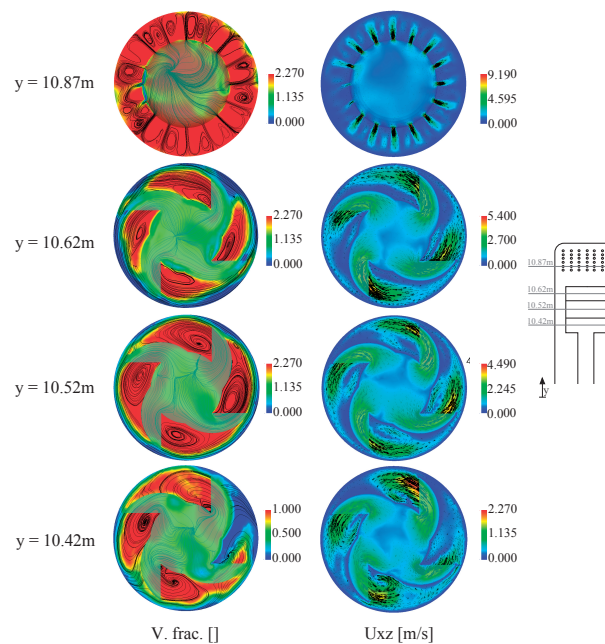Figure 8: Fields distribution over a mid-vertical plane cutting the riser.

Figure 9: Fields distribution over horizontal planes cutting the separator and the dryer.

Velocity profiles are also interesting to analyze (see figure 8); the maximum velocity of water is 4.5 m/s while steam velocity reaches $7.7 m/s$ on the top of the riser. Patterns are very similar, thus showing that the water is dragged by the steam with a velocity rate of 1.5 approximately. The baffles represent a barrier for the vapor rising. As can be noted, the flow through the connection holes is quite higher, especially for the first two holes. The last figure corresponds to the pressure distribution. Although the low liquid velocity in the pre-heater zone, there is a higher pressure drop caused by the large amount of baffles (22). Downstream the pre-heater, the connection holes equalize the pressure. The local pressure drops caused by the support baffles can also be identified. Almost the totality of the SG pressure drop is consequence of the hindering way caused by the baffles in the riser.

The downcomer flow is driven by the weight of the liquid column against the bottom riser pressure. Therefore, it should be emphasized that the agreement on the re-circulation rate m_{re} is mainly a consequence of the right pressure drops as long as the use of suitable interfacial force models.

It is of special significance the visualization of the flow inside the cyclone and the dryer. Figure 9 displays the streamlines, void fraction and the magnitude and direction of the horizontal velocity at four cross cut planes. The three lower planes (y = 10.62m, y = 10.52m and y = 10.42 m) intersect each one of the three cyclone stages while the upper plane cuts just a set of dryer orifices (The picture on the right sketches the plane locations). The three cyclone stages seem to work similarly although the horizontal velocity (U_{xz}) gets higher from the first to the third cyclone stage. The steam filled almost all the separator and the liquid is confined behind the peripheral walls. Liquid is projected from the all mouthpieces towards the cyclone cup, although separation is more effective at the upper cyclone stage, which is evidenced by the higher liquid accumulation at wall. The four discharge mouthpieces of every stage have similar behavior with the exception of one first-stage s mouthpiece.

The upper picture is also interesting to analyze; The steam jets, crossing the dryer orifices, are enough accelerated to hit the external shell, inducing small vortexes (one for each orifice). These organized flow structures work such as small cyclones, separating the ultimate small

drops. The efficiency of the steam separator is very closer to 100%, which is in accordance with the expected.

To obtain the right separation of phases employing interpenetrating models such as the two-fluid Eulerian-Eulerian model is a challenging assignment because the rheology of the disperse phase as long as the interaction with the walls are poorly solved. In this sense, the interfacial effects terms play a crucial role in order to model the real phenomena. As above stated, in the separator the steam reaches high velocities and consequently the drag became significant. However, for separation purposes, the inertial force must be dominant to guarantee that drops reach the walls, forming liquid slugs, which easy fall down. To accomplish that the Tomiyama model combined with the blending model allowed to use different particles sizes for drops in steam and bubbles in water, thus improving phase decoupling in the separation but also allowing liquid drag in the riser. This is mainly because Tomiyama model gives lows drag coefficients (C_D) when the Reynolds number becomes closer to zero ($Re_d \to 0$) and consequently the gravity force becomes dominant.
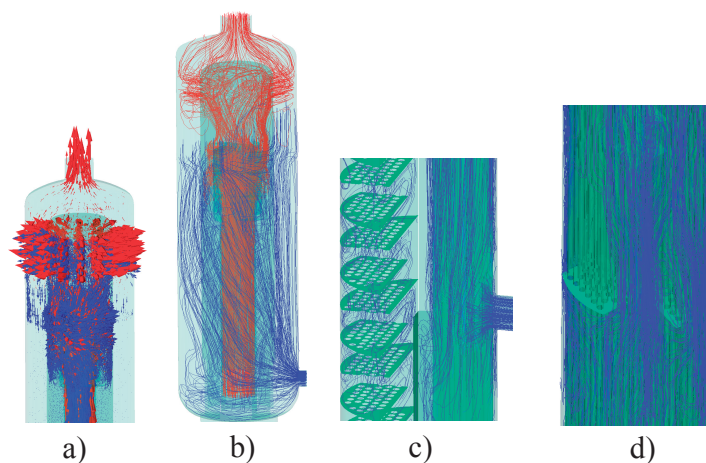

Figure 10: Flow distribution: a) Velocity vectors (water:blue, steam:red), b) streamlines (water:blue, steam:red), c) streamlines inside the pre-heater, d) streamlines around a baffle inside the riser.

Others flow characteristics are displayed in Figure 10. In picture 10-a and 10-b the velocity vectors and streamlines for steam (red) and liquid (blue) are drawn. For clarity the vectors corresponding to each phase were drawn with a different scale and filtered with a volume-threshold ($\alpha_1 \to 1$ for the water field and $\alpha_1 \to 0$ for the vapor field) in order to drawn vectors only where the corresponding phase is.

The majority of liquid is separated by the cyclone, although residual drops are dragged through the dryer holes, promoted by the steam acceleration. That projects the drops toward the most external wall, where they form clusters and fall by gravity. The picture clearly shows how the water falls down meanwhile the steam rises. In figure 10-b the steam streamlines display a swirl effect promoted by the centrifugal separator. This effect still remains downstream of the dryer holes.

Regarding the pre-heater (see picture 10-c), the large amount of baffles increases the path length and promotes cross flow enhancing the heat transfer. On the contrary, the support baffles in the riser induce stagnation of steam below them, whereas liquid accumulates above of them. In the same picture the downcomer flow entering to the bottom side of the riser is also showed. The flow discharged induces turbulent structures around the U-tubes. Picture 10-d shows how the streamlines straight ahead downstream and a fraction of the U-tubes remain unwetted by the
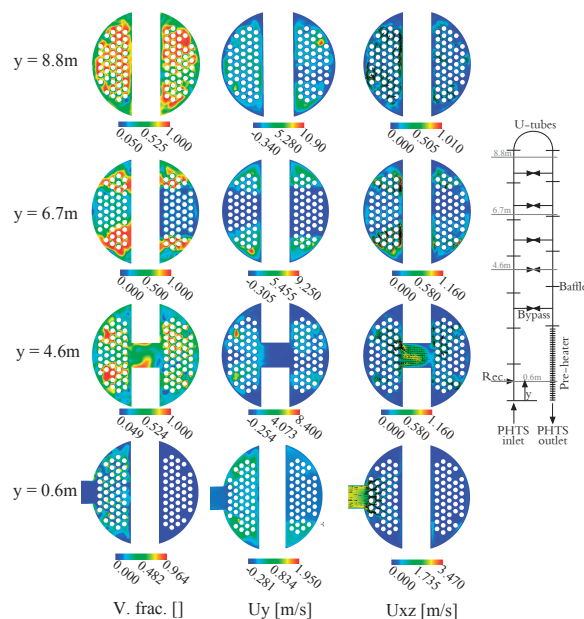
upward flow.

Figure 11: Horizontal cut planes: Void fraction, Vertical velocity and Horizontal velocity.

For the currently studied SG the number of U-tubes is lower than industrial devices. Therefore, the border effects should be more significant in this case. However, the present results would help to understand the complex two-phase flow that takes place around the tubes and baffles.

The void fraction and the vertical (U_y) and horizontal (U_{xz}) velocities are displayed in Figure 11 over four cross sectional horizontal planes. The bottom plane corresponds to the recirculation flow entrance height ($y = 0.6m$). As noted, only liquid water arrives from the downcomer but it is quickly mixed with the steam boiled in the tube bundle. The flow goes up through the periphery of the bundle while the horizontal flow, arriving from the downcomer, invades the center of the bundle. The horizontal velocity pattern is symmetric with maximum values up to $3m/s$. The second plane ($y = 4.6m$) is placed just at the second by-pass connection. At this height, steam clusters can be identified, thus inducing high local vertical velocities. It is also noticeable the flow crossing from the left to the right leg with horizontal velocities rising up to $0.5m/s$. The vertical velocity is progressively increased along the riser due to buoyancy but also due to the regime change (bubbly to slug). U_y locally grows up to $10m/s$ while U_{xz} remains lower than $1.1m/s$. In both legs the ascending flow is mainly in the U-tubes zone, with low velocity outside of the bundle.

The third plane ($y = 6.7m$) in Figure 11 is just above of two support baffles. It can be see how the flow distribution is strongly affected by them. The mixture flows mainly through the periphery hatches and the liquid accumulation above the baffles is also clearly observed. The horizontal velocity vectors show that the flow quickly returns to the central zone once it cross the baffles. the highest plane ($y = 8.8m$) was placed just before to the U-tube bends. In this case the steam fraction is upper than 50% in almost all the riser cross area. The flow is quite homogeneous in the vertical direction and velocities locally rise up to $10m/s$. In the other hand, the ratio between the horizontal and vertical velocity is around 0.1. However, the transverse motion around some U-tubes is quite intense. It can be concluded that the support baffles play a remarkable role on the flow distribution and should influence on the local heat transfer rate.
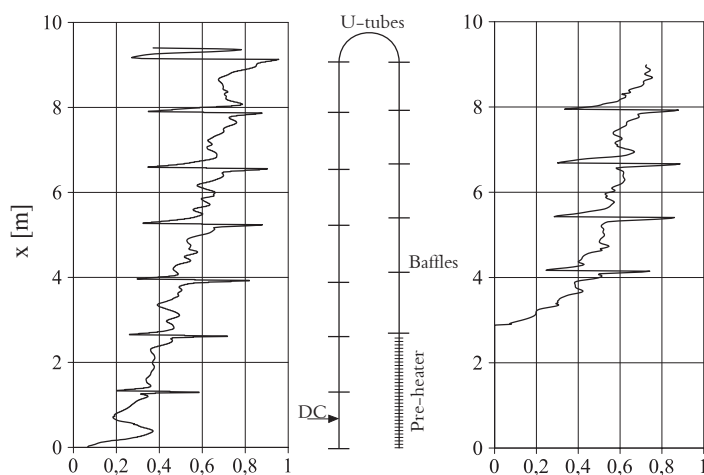
Figure 12: Cross average void fraction distribution: a) Left leg of the riser, b) Right leg of the riser.

The void fraction distribution (spatially-averaged along cross transverse planes) along the both riser legs is showed in Figure 12. The sharp variations are consequence of the baffles obstruction. As was pointed in preview sections, steam stagnates below the baffles whereas water accumulates above them. In the right leg, the pre-heater is completely fill of water but water quickly starts evaporating downstream it. In the left leg the downcomer entrance affect the void distribution. The re-circulated water quickly reduces the void fraction. The flow is mainly dominated by the bubbles buoyancy and the different weight of the water collapsed columns at riser and downcomer.

The pressure distribution along the riser is displayed in Figure 13. It is remarkable the large pressure drop along the pre-heater, which is responsible for more than a half of the overall pressure drop in the riser. In the raiser two patterns can be identified. The frictional pressure drop induced by the tube bundle and the form pressure drop caused by the baffles.
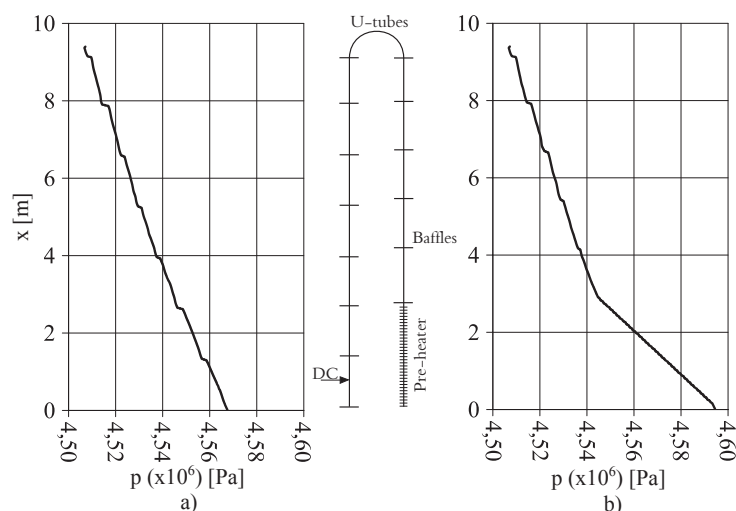

Figure 13: Pressure drop along the riser: a) Left leg, b) Right leg.

To complete the study, the figure 14 shows the velocity magnitude distribution in both legs. It must be mentioned that the vapor phase take the same value of the liquid when the void fraction tend to zero. It is evidenced in the pre-heater zone. In the left leg the velocity achieve negative

values below the downcomer injection. It is achieved by the vapor generation in this stagnant zone; the liquid down to this zone to guarantee the mass conservation. The low difference between the velocity phases demonstrate the high level of liquid drag induced by the vapor rising.
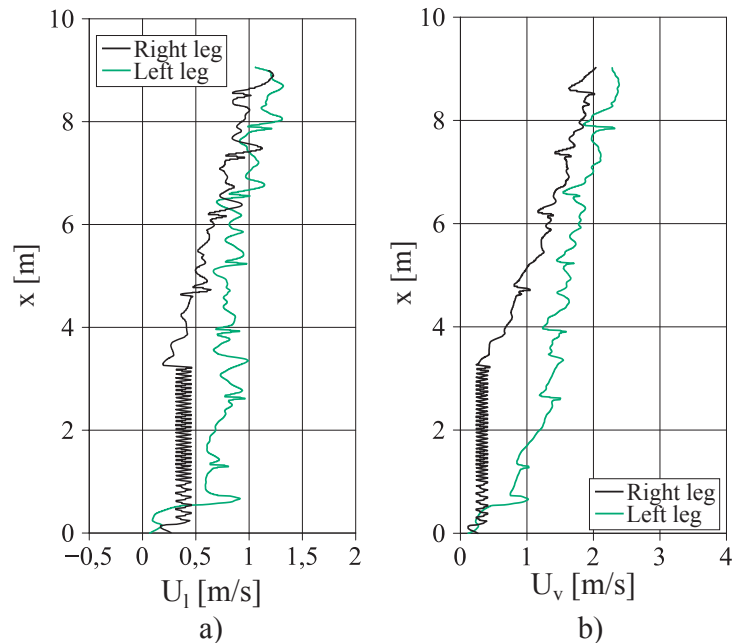

Figure 14: Velocity distribution: a) Liquid velocity, b) Vapor velocity.

5 CONCLUSIONS

A full geometry steam generator model was developed using three-dimensional Computational Fluid Dynamics. Simulations were focused on the secondary side in order to understand the complexity of the two-fluid flow. A blending model for interfacial momentum exchange was required to account for the different flow regimes that occurs along the steam generator.

Steady-state results such as the re-circulation rate, the void and pressure distributions was presented. Detailed visualization of the void and phase velocity fields near the baffles, the cyclone separator and dryer was carried out, identifying stagnation and detached flow zones, which can lead to temperature hot points, low heat transfer zones or vibration induced failure. The CFD model showed to be a very suitable tool for designing an assessing of steam generators as well as a data source for system code models. Future work should be dedicated to achieve a wall boiling model able to predict the local evaporation rate as a function of the primary to secondary heat transfer.

LIST OF SYMBOLS

α: Void fraction.

U: Velocity.

p: Pressure.

ρ: Density.

μ: Dynamic viscosity.

ν: Kinematic viscosity.

σ: Surface tension coefficient.

t: Time.

g: Gravitational acceleration.

τ: Laminar stress tensor.

R: Reynolds stress tensor.

M: Interfacial force per unit volume.

Γ: Mass transfer.

K: Interfacial constant coefficient.

C: Constant coefficient.

f: Blending factor.

d: Dispersed droplet-bubbly diameter.

L: Characteristic length.

λ_f: Friction factor.

ζ: Form loss coefficient.

I: Identity matrix.

n: Surface normal vector.

y: Wall distance.

$E_o = \frac{d_1^2 g \Delta \rho}{\sigma}$: Eotvos number.

$M_o = \frac{\mu_2^4 g \Delta \rho}{\rho_2^2 \sigma^3}$: Morton number.

$Re = \frac{UL}{\mu}$: Reynolds number.

Superscripts:

D: Drag force.

SL: Shear lift force.

WL: Wall lubrication force.

VM: Virtual mass force.

TD: Turbulent dispersion force.

T: Transposition.

Subscripts:

γ: Phase index.

1: Liquid phase.

2: Vapor phase.

$1, 2$: Liquid to vapor transfer.

$2, 1$: Vapor to liquid transfer.

r: Continuous-Dispersed relative value.

pd: Partially dispersed.

fd: Fully dispersed.

d: Dispersed.

w: Wall.

eff: Effective.

LIST OF ACRONYMS

P: Pipe.
J: Junction.
B: Branch.
S: Steam separator.
VLV: Valve.
HS: Heat structure.
TDJ: Time dependent junction.
TDV: Time dependent volume.
CFD: Computational fluid dynamics.
CHT: Conjugated heat transfer.
LFC: Loss of forced convection.
LOCA: Loss of coolant accident.
NPP: Nuclear power plant.
PHWR: Pressure heavy water reactor.
PWR: Pressure water reactor.
SG: Steam generator.
OFM: OpenFoam model.
SCM: System code.

REFERENCES

Antal S., Lahey Jr R., and Flaherty J. Analysis of phase distribution in fully developed laminar bubbly two-phase flow. *International Journal of Multiphase Flow*, 17(5):635–652, 1991.

Behzadi A., Issa R., and Rusche H. Modelling of dispersed bubble and droplet flow at high phase fractions. *Chemical Engineering Science*, 59(4):759–770, 2004.

Clift R., Grace J., Weber M., and Clift R. *Bubbles, drops, and particles*, volume 3. Academic press New York, 1978.

Cong T., Tian W., Qiu S., and Su G. Study on secondary side flow of steam generator with coupled heat transfer from primary to secondary side. *Applied Thermal Engineering*, 61(2):519–530, 2013.

Drew D. and Lahey Jr R. The virtual mass and lift force on a sphere in rotating and straining inviscid flow. *International Journal of Multiphase Flow*, 13(1):113–121, 1987.

Drew D. and Passman S. *Theory of multicomponent fluids*. Springer, 1999.

Enwald H., Peirano E., and Almstedt A. Eulerian two-phase flow theory applied to fluidization. *International Journal of Multiphase Flow*, 22:21–66, 1996.

Evje S. and Fjelde K. Hybrid flux-splitting schemes for a two-phase flow model. *Journal of Computational Physics*, 175(2):674–701, 2002.

Ferng Y.M. Investigating the distribution characteristics of boiling flow and released nuclide in the steam generator secondary side using cfd methodology. *Annals of Nuclear Energy*, 34(9):724–731, 2007.

Ferng Y.M. and Chang H.J. Cfd investigating the impacts of changing operating conditions on the thermal-hydraulic characteristics in a steam generator. *Applied Thermal Engineering*, 28(5):414–422, 2008.

Frank T., Zwart P., Krepper E., Prasser H., and Lucas D. Validation of cfd models for mono- and polydisperse air–water two-phase flows in pipes. *Nuclear Engineering and Design*, 238(3):647–659, 2008.

Gidaspow D. *Multiphase flow and fluidization: continuum and kinetic theory descriptions*. Academic Pr, 1994.

Hänsch S., Lucas D., Krepper E., and Höhne T. A multi-field two-fluid concept for transitions between different scales of interfacial structures. *International Journal of Multiphase Flow*, 47:171–182, 2012.

Hill D.P. *The computer simulation of dispersed two-phase flow*. Ph.D. thesis, University of London, 1998.

Ishii M. Thermo-fluid dynamics of two-phase flow. Recon technical report a, NASA STI, 1975.

Ishii M. and Zuber N. Drag coefficient and relative velocity in bubbly, droplet or particulate flows. *AIChE Journal*, 25(5):843–855, 1979.

Koncar B. Kljenak I. and Mavko B. Modelling of local two-phase flow parameters in upward subcooled flow boiling at low pressure. *International Journal of Heat and Mass Transfer*, 47:1499–1513, 2004.

Krepper E., Koncar B., and Egorov Y. Cfd modelling of subcooled boilingâATconcept, validation and application to fuel assembly design. *Nuclear Engineering and Design*, 237(7):716–731, 2007.

Lahey R.T. The simulation of multidimensional multiphase flows. *Nuclear Engineering and Design*, 235(10):1043–1060, 2005.

Li Y., Yang Y., and Sun B. Numerical investigation of thermal–hydraulic characteristics in a steam generator using a coupled primary and secondary side heat transfer model. *Annals of Nuclear Energy*, 55:258–264, 2013.

Márquez Damián S. *An extended mixture model for the simultaneous treatment of short and long scale interfaces*. Ph.D. thesis, Ph. D. thesis, FICH, Universidad Nacional del Litoral, Santa Fe, Argentina, 2013.

Marschall H. *Towards the Numerical Simulation of Multi-Scale Two-Phase Flows*. Ph.D. thesis, Technische Universität München, 2011.

Mostafa G.S. Two-phase flow, boiling and condensation in conventional and miniature systems. 2008.

Pellacani F., Mestre S.M., Vicent S.C., and Juan R.M. Cfd modeling of subcooled boiling in vertical bubbly flow condition using ansys cfx 12. pages 1153–1162. 2010.

Rämä T., Toppila T., Pattikangas T., Niemi J., and Hovi V. Cfd-simulation of the vver-440 steam generator with porous media model. *The 8th Int. Semin. on Horizontal Steam Generators, Podolsk, Russia*, 2010.

Reynolds O. On the dynamical theory of incompressible viscous fluids and the determination of the criterion. *Philosophical Transactions of the Royal Society of London.*, 186:123–164, 1895.

Rusche H. *Computational Fluid Dynamics of Dispersed Two-Phase Flows at High Phase Fractions*. Ph.D. thesis, Imperial college of science, technology and medicine, 2002.

Sar S., Ergün Ş., Bar k M., Kocar C., and Sökmen C.N. Modeling of isothermal bubbly flow with nterfacial area transport equation and bubble number density approach. *Annals of Nuclear Energy*, 36(2):222–232, 2009.

Schiller L. and Naumann A. Uber die grundlegenden berechnungen bei der schwerkraftaufbereitung. *Ver. Deut. Ing*, 77(318-320):33, 1933.

Stosic Z. and Stevanovic V. Advanced three-dimensional two-fluid porous media method for transient two-phase flow thermal-hydraulics in complex geometries. *Numerical Heat Transfer: Part B: Fundamentals*, 41(3-4):263–289, 2002.

Tolubinsky V. and Kostanchuk D. Vapour bubbles growth rate and heat transfer intensity at

subcooled water boiling. In *Proceedings of the 4th International Heat Transfer Conference*, volume 5. 1970.

Tomiyama A. Drag, lift and virtual mass force acting on a single bubble. In *3rd International Symposium on Two-Phase Flow Modelling and Experimentation, 2004*. 2004.

Tomiyama A., Kataoka I., Zun I., and Sakaguchi T. Drag coefficients of single bubbles under normal and micro gravity conditions. *JSME International Journal Series B Fluids and Thermal Engineering*, 41(2):472–479, 1998.

Tomiyama A., Sakoda K., Hayashi K., Sou A., Shimada N., and Hosokawa S. Modeling and hybrid simulation of bubbly flow. *Multiphase Science and Technology*, 18(1):73, 2006.

Unal H. Maximum bubble diameter, maximum bubble-growth time and bubble-growth rate during the subcooled nucleate flow boiling of water up to 17. 7 mn/sq m. *International Journal of Heat and Mass Transfer*, 19:643–649, 1976.

Wang S., Lee S., Jones O., and Lahey R. 3-d turbulence structure and phase distribution measurements in bubbly two-phase flows. *International Journal of multiphase flow*, 13(3):327–343, 1987.

Weller H. Derivation, modelling and solution of the conditionally averaged two-phase flow equations. Technical Report, Technical Report TR/HGW/02, Nabla Ltd, 2002.

Zalesak S. Fully multidimensional flux-corrected transport algorithms for fluids. *Journal of computational physics*, 31(3):335–362, 1979.

Zhang G., Zhang Y., Yang Y., Li Y., and Sun B. Dynamic heat transfer performance study of steam generator based on distributed parameter method. *Annals of Nuclear Energy*, 63:658–664, 2014.